Photon Migration in Tissue

2

Masatsugu Niwayama and Yutaka Yamashita

2.1 Introduction

Although many researchers have attempted to determine the absolute value of tissue oxygenation using time-resolved spectroscopy, spatially resolved spectroscopy (SRS), phase-modulated spectroscopy, and continuous-wave spectroscopy (CWS) (see Chap. 1), correction methods are necessary for quantitative measurement. For example, such overlying tissues as skulls and subcutaneous adipose tissues greatly affect the measurement sensitivity of near-infrared spectroscopy (NIRS). Therefore, analysis of photon migration is important in obtaining accurate absolute measurements. Several researchers have derived equations for the temporal and spatial dependence of diffusely reflected light in a turbid medium [1–8]. Analytical solutions of diffusion theory are widely used to quantify the optical properties of homogeneous media. Kienle et al. [8] theoretically examined propagation in a two-layered medium using a diffusion theory. In addition, Monte Carlo methods have also frequently been used to simulate photon migration [9–16]. In 1983 Wilson et al. [9] presented a Monte Carlo model to examine light propagation in tissues. Van der Zee and Delpy [10] proposed a new method for calculating absorption during light propagation. Many researchers have analyzed various models that simulate actual tissue structure. For example, Wang et al. [11] performed Monte Carlo modeling of photon transport in multilayered tissues. Okada et al. [12] investigated the influence of cerebrospinal fluid and the skull on cerebral oxygenation measurement using a Monte Carlo method. Yamamoto and Niwayama [13, 14] also performed a Monte Carlo simulation of muscle oxygenation measurement with a four-layered model and demonstrated a simple correction method for CWS. Additionally, Boas et al. [15, 16] reported high-speed analysis of three-dimensional photon migration using graphics processing units.

In this chapter we present methods for analyzing photon migration in tissues. The effects of inhomogeneities on NIRS, determined by photon migration analysis are also described.

M. Niwayama, Ph.D. (✉)
Department of Electrical and Electronic Engineering, Shizuoka University, 3-5-1 Johoku, Nakaku, Hamamatsu, Shizuoka 432-8561, Japan
e-mail: tmniway@ipc.shizuoka.ac.jp

Y. Yamashita, BS
Central Research Laboratory, Hamamatsu Photonics KK, 5000 Hirakuchi, Hamakita-ku, Hamamatsu City, Shizuoka 434-8601, Japan
e-mail: yutaka@crl.hpk.co.jp

T. Jue and K. Masuda (eds.), *Application of Near Infrared Spectroscopy in Biomedicine*, Handbook of Modern Biophysics 4, DOI 10.1007/978-1-4614-6252-1_2,

2.2 Photon Diffusion Theory

2.2.1 Homogeneous Media

Exact analytical solutions of the radiation transport equation have been found in only a few special cases [1], and it is a formidable task to perform numerical calculations using the discrete-ordinate method, even for simple geometries. Thus, many investigators have used angle-independent solutions of a transport equation based on diffusion (or P1) approximation to model light scattering in biological tissues. The radiation transport equation is given as

$$\frac{1}{c}\frac{\partial I(\mathbf{r},\mathbf{s},t)}{\partial t} = -\boldsymbol{S}\cdot\nabla I(\boldsymbol{r},\boldsymbol{s},t) - (\mu_\mathrm{s}+\mu_\mathrm{a})I(\boldsymbol{r},\boldsymbol{s},t) + \frac{\mu_\mathrm{s}}{4\pi}\int_{4\pi} I(\boldsymbol{r},\boldsymbol{s},t)p(\boldsymbol{s},\boldsymbol{s}')ds' + q(\boldsymbol{r},\boldsymbol{s},t), \tag{2.1}$$

where $I(\boldsymbol{r},\boldsymbol{s},t)$ is the average power flux density at point $\boldsymbol{r}$ in the direction of unit vector $\boldsymbol{s}$ (Fig. 2.1), $p(\boldsymbol{s},\boldsymbol{s}')$ is the scattering phase function, and $q(\boldsymbol{r},\boldsymbol{s},t)$ is the source function (the number of photons injected into a unit volume).

In a diffusive process, the following assumptions are made: (1) scattering dominates absorption in the medium, (2) scattering is nearly isotropic, and (3) measurements are made at a sufficient distance from sources and boundaries. Under these assumptions, the diffusion equation can be derived from the radiative transport equation as follows:

$$\frac{1}{c}\frac{\partial\phi(r,t)}{\partial t} - D\nabla^2\phi(r,t) + \mu_\mathrm{a}\phi(\boldsymbol{r},t) = S(\boldsymbol{r},t), \tag{2.2}$$

where total energy fluence rate $\phi(\boldsymbol{r},t)$, isotropic source $S(\boldsymbol{r},t)$, and diffusion constant D are given by

$$\phi(\boldsymbol{r},t) = \int_{4\pi} I(\boldsymbol{r},\boldsymbol{s},t)\ ds, \tag{2.3}$$

$$S(\boldsymbol{r},t) = \int_{4\pi} q(\boldsymbol{r},\boldsymbol{s},t)\ ds, \tag{2.4}$$

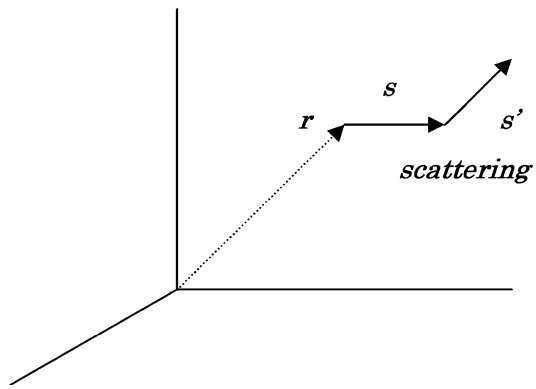

Fig. 2.1 Photon transport

$$D = \frac{1}{3(\mu'_s + \mu_a)}. \tag{2.5}$$

Patterson et al. [4] derived the following equation for the temporal and spatial dependence of diffusely reflected light (reflectance R) in a semiinfinite medium:

$$R(\rho, t) = (4D\pi c)^{-3/2} t^{-5/2} z_0 \exp(-\mu_a ct) \exp\left(-\frac{z_0^2 + \rho^2}{4Dct}\right). \tag{2.6}$$

Integration over a time t yields [6]

$$R(\rho) = \frac{z_0}{2\pi}\left(\mu_{\text{eff}} + \frac{1}{\sqrt{z_0^2 + \rho^2}}\right)\frac{\exp\left(-\mu_{\text{eff}}\sqrt{z_0^2 + \rho^2}\right)}{z_0^2 + \rho^2}. \tag{2.7}$$

If $\rho > z_0$, reflectance R is given by

$$R(\rho) = \frac{1}{2\pi\mu'_s\rho^2}\left(\mu_{\text{eff}} + \frac{1}{\rho}\right)\exp(-\mu_{\text{eff}}\rho), \tag{2.8}$$

2.2.2 Inhomogeneous Media

Several investigators have investigated a solution for a diffusion equation for layered turbid media. Takatani et al. [3] derived analytical expressions for steady-state reflectance by using Green's functions to solve the diffusion equation, and Dayan et al. [5] used Fourier and Laplace transforms to obtain solutions for steady-state and time-resolved reflectances. Kienle et al. [8] solved the diffusion equation using a Fourier transform approach for a two-layered turbid medium as follows:

$$R(\rho) = 0.118\Phi_1(\rho, z = 0) + 0.306\frac{\partial}{\partial z}\Phi_1(\rho,z)|_{z=0}, \tag{2.9}$$

$$\Phi_1(\rho,z) = \frac{1}{2\pi}\int_0^\infty \phi_1(z) s J_0(s\rho)\, ds, \tag{2.10}$$

$$\phi_1(z) = \frac{\sinh(\alpha_1(z_b + z_0))}{D_1\alpha_1}\frac{D_1\alpha_1\cosh(\alpha_1(l - z)) + D_2\alpha_2\sinh(\alpha_1(l - z))}{D_1\alpha_1\cosh(\alpha_1(l + z_b)) + D_2\alpha_2\sinh(\alpha_1(l + z_b))} - \frac{\sinh(\alpha_1(z_0 - z))}{D_1\alpha_1}, \tag{2.11}$$

where J_0 is the zeroth-order Bessel function, D_i is the diffusion constant for layer i, ${\alpha_i}^2 = (D_i s^2 + \mu_{ai})/D_i$, l is the thickness of the first layer, z_0 is the isotropic source depth, $z_b = (1 + R_{\text{eff}})D_1/(1 - R_{\text{eff}})$, and R_{eff} is 0.493 [7], for a refractive index of 1.4. The reflectance calculated from this solution agreed well with that computed by a Monte Carlo simulation. Although this approach was similar to that proposed by Dayan, it was more accurate and considered mismatches in the refraction index at a tissue surface.

The finite-element method (FEM) is the most common method for numerically solving the diffusion equation for arbitrarily shaped inhomogeneous media. Analysis of light propagation using the FEM [17] is based on the discrete diffusion equation. Furthermore, the model for the FEM is divided into a large number of volume or area elements, each of which has its individual set of optical properties (absorption and scattering coefficients). Solutions are found simultaneously at all nodes of the finite-element mesh by inverting the associated matrix. The photon densities of the individual elements are computed from the node values via an interpolation scheme, which ensures continuity of the overall solution. Although the FEM is fast compared to the Monte Carlo method (see Sect. 2.3), it requires a long time and a large amount of computer memory for calculating a three-dimensional model having a complex shape.

2.3 Monte Carlo Methods

The statistical behavior of random walks has been used to examine light propagation in a turbid medium. Bonner et al. [18], Nossal et al. [19], and Taitelbaum et al. [20] modeled the kinetics of photon migration in a two-layered medium in terms of a random walk on a discrete lattice, where the lattice spacing is equivalent to the root-mean-square distance between scattering events, and absorption occurs in the intervening space. Taitelbaum et al. have found that if the upper layer has a higher absorption than the lower layer, the absorption coefficients of the two layers can be determined from a surface reflectance profile. In contrast, when the upper layer has a lower absorption than the lower layer it is difficult to estimate the optical properties of the two regions.

The Monte Carlo technique has been widely applied to radiation transport studies. This technique is based on the stochastic nature of radiation interactions. The probability of a photon being scattered after traveling a distance dl is defined as

$$p(l)\ dl = \exp(-\mu_s l)\ dl. \tag{2.12}$$

Thus, the cumulative probability of scattering after a distance l is traveled is

$$\int_0^l p(l')\ dl' = 1 - \exp(-\mu_s l) \equiv r, \tag{2.13}$$

where $0 < r < 1$ is a uniformly distributed random number; therefore, $1 - r$ equals r. The path length between scattering events is calculated as

$$l = -\frac{1}{\mu_s} \ln(1 - r) = -\frac{1}{\mu_s} \ln(r). \tag{2.14}$$

Wilson et al. developed a Monte Carlo model to examine propagation in tissues [9]. In this model (Fig. 2.2a), at the absorption/scattering point, the photon is assumed to deposit a fraction μ_a/μ_t of its current intensity I_i (initially set equal to 1) as absorbed energy and to emerge from the point with a weighting factor:

$$I_{i+1} = (\mu_s/\mu_t) I_i. \tag{2.15}$$

The direction of the scattered photon is selected from a random distribution such that the probability per unit solid angle is the same in all directions. In contrast, van der Zee and Delpy [10] proposed

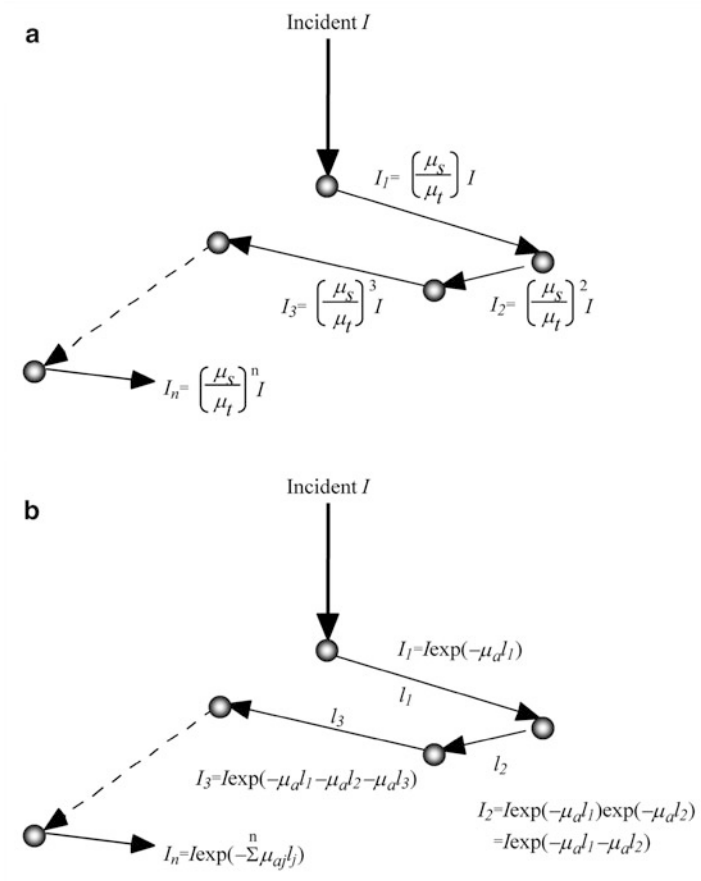

Fig. 2.2 Monte Carlo models reported by Wilson et al. (**a**) and van der Zee and Delpy (**b**)

a new method for calculating absorption in media. In their method absorption occurs at the molecular level and is therefore equal to $\exp(-\mu_a l)$, as shown in Fig. 2.2b. It is shown here that these two methods are essentially the same. From Eq. 2.15, detected light intensity I is expressed as

$$I = (\mu_s/\mu_t)^N I_0 = (1 - \mu_a/\mu_t)^N I_0, \tag{2.16}$$

where I_0 is the initial light intensity and N is the number of scattering events.

The number of scattering events N is equal to $\mu_s' l$. Maclaurin expansion yields the following expression:

$$\begin{aligned}\left(1-\frac{\mu_a}{\mu_t}\right)^{\mu'_s l} = 1 - \left(\mu'_s l\frac{\mu_a}{\mu_t}\right) + \frac{\mu'_s l(\mu'_s l-1)}{2!}\left(\frac{\mu_a}{\mu_t}\right)^2 - \frac{\mu'_s l(\mu'_s l-1)(\mu'_s l-2)}{3!}\left(\frac{\mu_a}{\mu_t}\right)^3 \\ + \cdots + (-1)^n \frac{\mu'_s l(\mu'_s l-1)\cdots(\mu'_s l-n+1)}{n!}\left(\frac{\mu_a}{\mu_t}\right)^n + \cdots\end{aligned} \tag{2.17}$$

for $\mu_a/\mu_s < 1$.

In contrast, detected light intensity I in the model proposed by van der Zee and Delpy is expressed as

$$I = I_0 \exp(\mu_a l). \tag{2.18}$$

Maclaurin expansion yields the following:

$$\exp(-\mu_a l) = 1 - (\mu_a l) + \frac{1}{2!}(\mu_a l)^2 - \frac{1}{3!}(\mu_a l)^3 + \cdots \tag{2.19}$$

For all $\mu_a l$.

Hence, Eqs. 2.17 and 2.19 show that the model proposed by van der Zee and Delpy is almost identail to of Wilson et al.

2.4 Models for Monte Carlo Simulation

The three-dimensional models shown in Fig. 2.3 were used to simulate light propagation within a layered structure. A two-layered model (fat and muscle layers) was used initially. To examine the effect of the skin, a four-layered model (epidermis, dermis, fat, and muscle layers) was also employed. The thicknesses of the epidermis and dermis were 60 μm and 1 mm, respectively. The thickness of the fat

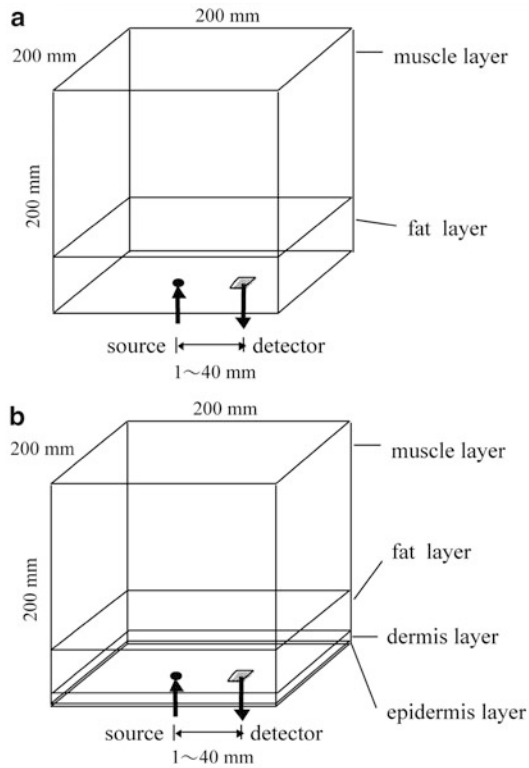

Fig. 2.3 Two- (**a**) and four-layered (**b**) models

Table 2.1 Reduced scattering coefficient and absorption coefficient of each layer

Layer	Reduced scattering coefficient (mm^{-1})	Absorption coefficient (mm^{-1})	References
Epidermis	5.0	5.9	[21]
Dermis	1.3	0.03	[22]
Fat	1.2	0.003	[23]
Muscle	0.6	0.02	[24]

layer varied from 0 to 14 mm, while the total thickness of the four layers was maintained at 200 mm. The size of the model was 200 mm × 200 mm × 200 mm. The source–detector distance varied from 20 to 40 mm.

Calculations were performed by the algorithm [10] presented below. Isotropic scattering length L_i of the ith path was determined by Eq. 2.20, as described in Sect. 2.3, as follows:

$$L_i = -\ln(R)/\mu'_s, \tag{2.20}$$

where R is a random number between 0 and 1 and μ'_s is the reduced scattering coefficient of each layer. When a photon crossed the boundary between the fat and muscle layers, L_i was corrected by the ratio of the reduced scattering coefficients of both layers. Because biological tissues are strong multiple-scattering media, isotropic scattering was assumed. The successive paths of a photon in the two layers were stored, and the relative intensity of a detected photon was calculated by Eq. 2.21, which was derived from Eq. 2.18, as

$$I/I_0 = \exp(-\mu_{af}\ \Sigma L_i - \mu_{am}\ \Sigma L_j) \tag{2.21}$$

where μ_{af} and μ_{am} are the absorption coefficients of the fat and muscle layers, respectively. In the simulation, 10^8 photons were vertically injected into the fat layer at the source point. The size of the detector was assumed to be 5 mm × 4 mm, which corresponds to the size of the photodiode (S2386-45K, Hamamatsu Photonics KK).

The optical properties of the simulated tissues were determined on the basis of values in the literature [21–23]. The reduced scattering coefficients and absorption coefficients of each layer are shown in Table 2.1.

2.5 Calculation of Spatial Sensitivity

Photon migrations within a fat layer and a muscle layer were obtained by Monte Carlo simulation. The spatial sensitivities at different tissue sites, showing the contribution of different tissue sites to the intensity of the detected light, were also calculated. The spatial sensitivity is also equivalent to the mean optical path length of each cell defined at the sites of interest. The model was divided into small cubes, called cube "cells," as shown in Fig. 2.4. Each cube was 1 mm × 1 mm × 1 mm in size. The mean path length $<L>$ of a cell was calculated by $\sum(L_iI_i)/\sum I_i$, where L_i is the path length of the ith photon in the cell and I_i is the final intensity of the ith photon at a detector. To focus on the spatial sensitivities in the x- and z-axis directions, the sensitivity values of the cell were summed up in the y-axis direction and illustrated. The distribution of sensitivities in the x-y plane at each layer was also obtained.

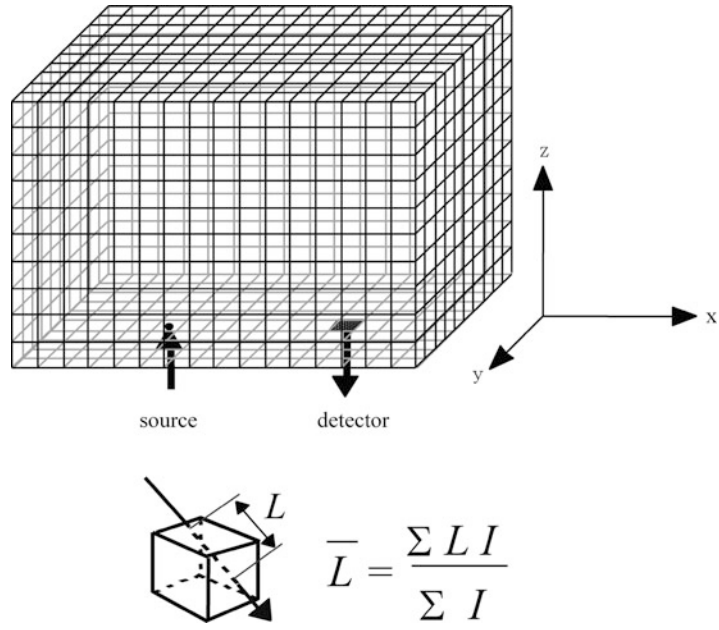

Fig. 2.4 Model divided into cells and calculation of mean optical path length $<L>$

2.6 Photon Migration in Layered Tissues

Figure 2.5 shows light propagation within a fat layer and a muscle layer obtained by simulation using a two-layered model. This graphic shows the distribution of spatial sensitivities (i.e., the mean optical path length of each cell). The sensitivity distribution has a banana shape. Sites close to the source or the detector have the greatest effect on the detected light. When the fat layer is 3 mm thick, the spatial sensitivity within the muscle layer is relatively high. In contrast, the spatial sensitivity of the muscle layer is greatly diminished when the fat layer is 10 mm thick. Because the absorption coefficient of a fat layer is much lower than that of a muscle layer, the detected light consists mainly of light passing through the fat layer when it is thick. Light that penetrates into the muscle and reaches the detector is greatly reduced. This implies that the presence of a fat layer greatly affects measurement sensitivity.

Figure 2.6 shows the sensitivity distribution in the x–y plane at a source–detector separation of 30 mm. The distribution is spindle shaped and is 10 mm wide in the y-axis direction. These results are important for the basic design of an imaging system.

2.7 Effect of Fat Layer

Figure 2.7 shows the mean optical path lengths $<L_m>$ in a muscle layer at source–detector separations of 20, 30, and 40 mm, which were obtained by Monte Carlo simulation. The presence of a fat layer greatly decreases $<L_m>$. When the source–detector separation is small, $<L_m>$ becomes zero even for a relatively thin fat layer.

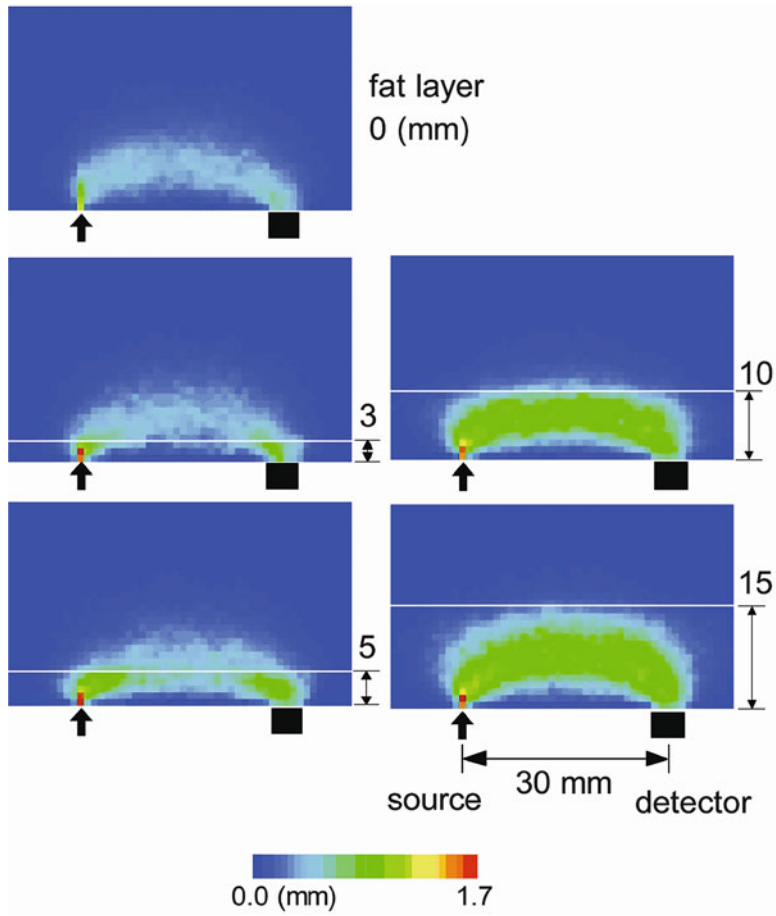

Fig. 2.5 Spatial sensitivities for various fat layer thicknesses

Figure 2.8 shows the optical path length in a muscle layer obtained from a Monte Carlo simulation in which the absorption coefficient for the muscle was 0.02 mm^{-1}. The relationship between normalized optical path length S_{muscle} and fat layer thickness h is expressed by the following equation:

$$S_{muscle} = \exp\left\{-\left(\frac{h}{A}\right)^2\right\}. \tag{2.22}$$

The constant A has the values 6.9, 8.0, and 8.9 for source–detector distances of 20, 30, and 40 mm, respectively. The value of S_{muscle} can be determined only by using the h value previously measured by ultrasonography. Then, the changes in hemoglobin concentration obtained using CW-NIRS can be corrected by dividing them by S_{muscle}. In in vivo tests the average value of resting oxygen consumption in the forearms of the subjects was 0.13 $\pm$ 0.02 ml 100 g^{-1} min^{-1} (mean $\pm$ SD) after correction. Before correction of a fat layer, the mean value of oxygen consumption was about 50% smaller than the reported values [25, 26], and the coefficient of variation showed great dispersion.

A decrease in the measurement sensitivity is caused by an increase in the proportion of light that directly reaches the detector through the fat layer. Therefore, not only the measurement sensitivity but also the intensity of detected light depends on fat layer thickness. Therefore, the detected light intensity was recorded and plotted against fat layer thickness, as depicted in Fig. 2.9. Detected light intensity increased with fat layer thickness. Light intensity is plotted on a logarithmic scale. When the fat layer is

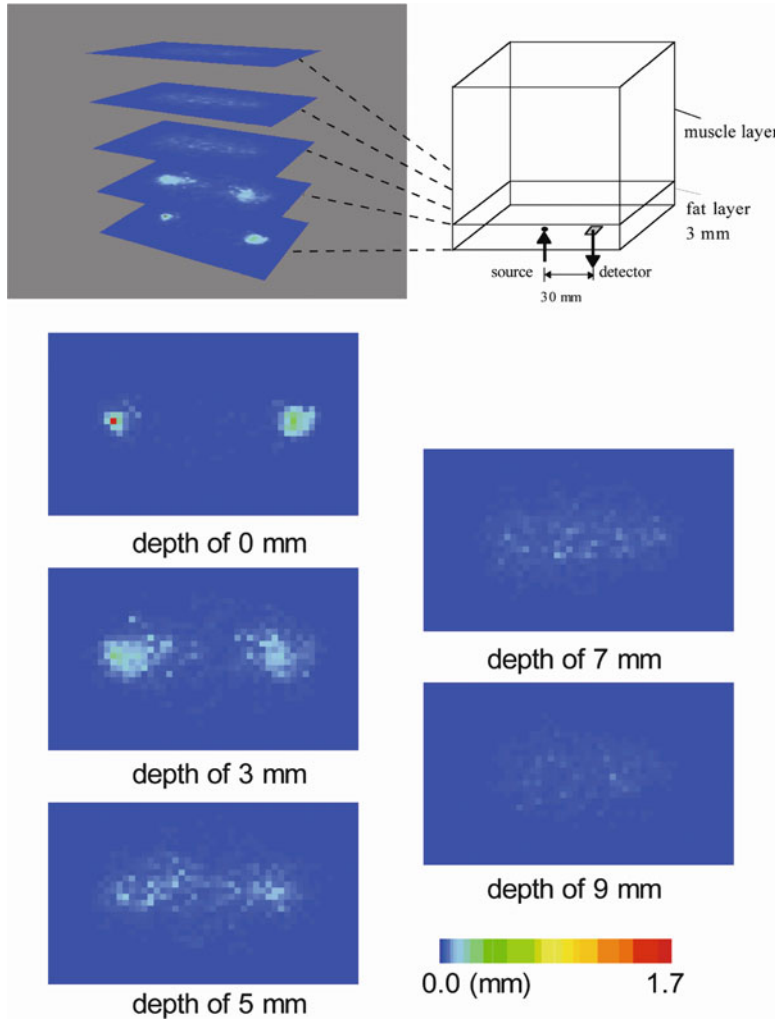

Fig. 2.6 Spatial sensitivities at depths of 0–9 mm. Fat layer thickness, 3 mm; source–detector separation, 30 mm

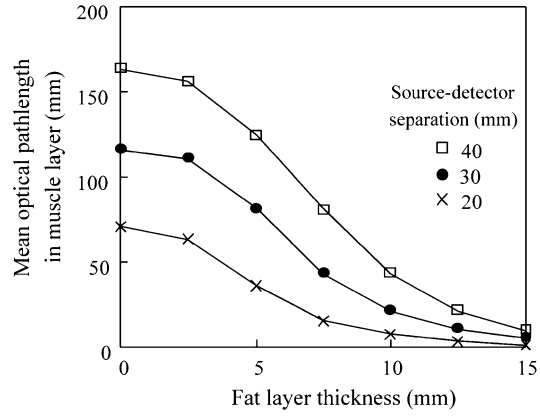

Fig. 2.7 Decrease in measurement sensitivity because of presence of a fat layer. Mean optical path length in the muscle layer was calculated by Monte Carlo simulation

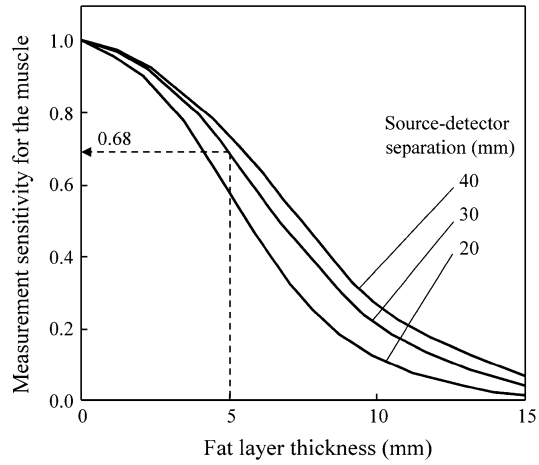

Fig. 2.8 Measurement sensitivity for muscle in CW-NIRS calculated by Monte Carlo simulation

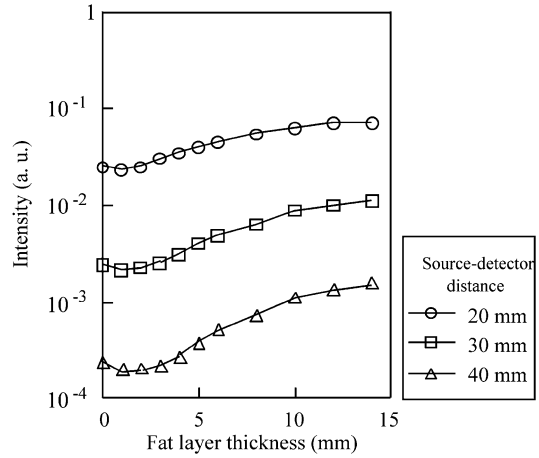

Fig. 2.9 Relationship between detected light intensity and fat layer thickness in the simulation results

thicker than 9 mm, detected light intensity increases slightly and reaches a maximum, corresponding to the light intensity detected in a fat layer whose thickness is regarded as infinite. Therefore, when the source–detector separation is small, the maximum intensity is reached at a small fat layer thickness. For a fat layer thickness of less than 3 mm, an upward tendency appears around a fat layer thickness of zero. This is thought to be due to an increase in light propagating into a muscle layer and light backscattered from this layer to a detector, because attenuation due to scattering in a fat layer diminishes with decreasing fat layer thickness.

2.8 Effect of Skin

The effect of the skin on muscle oxygenation measurement was also examined by simulation. Figure 2.10a shows the relationship between the mean optical path length in a muscle layer and the thickness of a fat layer at various source–detector distances. When the source–detector distance is less

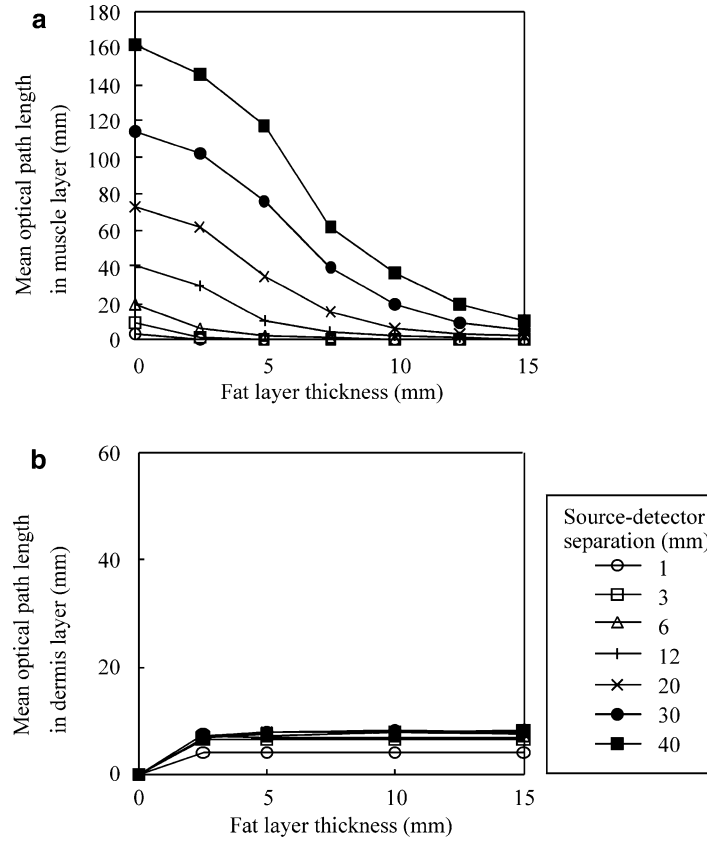

Fig. 2.10 Relationship between fat layer thickness and mean optical path length in a muscle layer (**a**) and in a dermis layer (**b**)

than 3 mm and the fat layer is thicker than 3 mm, the mean optical path length in the muscle layer is almost zero. Thus, there is almost no sensitivity toward changes in muscle oxygenation under this condition. The mean optical path length in the dermis is almost constant when the source–detector distance and fat layer thickness are larger than 3 mm, as shown in Fig. 2.10b. These results suggest that the effect of skin blood flow can be eliminated by using the signal obtained at a 3-mm separation. Subtraction of optical density (OD) at the 3-mm separation from that at larger separations yields the change in muscle oxygenation without the effect of the skin and without decreasing sensitivity to the muscle. Thus, the optimal source–detector separation for eliminating the effect of the skin is likely to be 3 mm.

However, the effect of the skin on change in OD was 8% or less compared to that of muscle at the 30-mm separation, and there was little change in blood volume of the skin because the optical probe was pressed lightly on the body surface in in vivo measurements. Thus, the effect of blood in the skin can be ignored when the source–detector separation is large (>20 mm).

2.9 Analysis of Time-Resolved Measurement

Diffuse optical tomography using time-resolved reflectance has been widely studied as a useful technique for noninvasive measurement of internal physiological information. Analysis of a time-resolved photon path distribution is essential for conducting image reconstruction using optical tomography. Figure 2.11 shows the impulse response without absorption and the photon path distributions

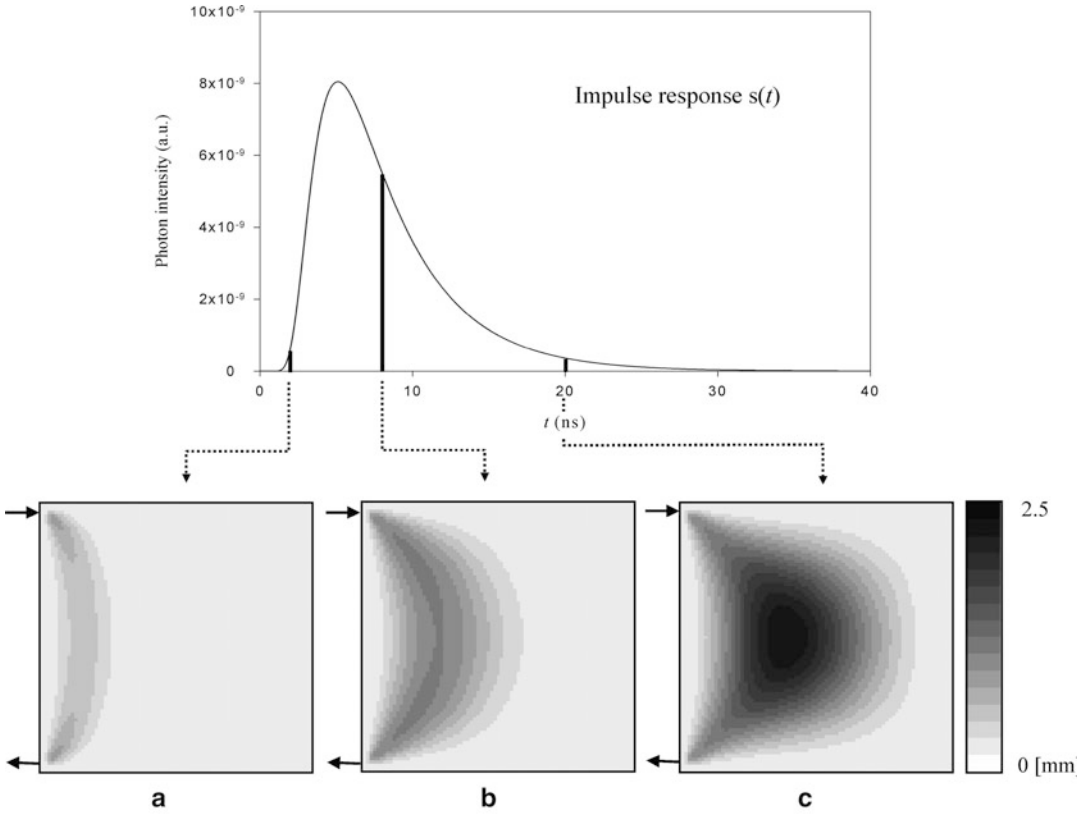

Fig. 2.11 Impulse response and photon path distributions at $t = 2$ ns (**a**), $t = 8$ ns (**b**), and $t = 20$ ns (**c**)

at 2, 8, and 20 ns, calculated using diffusion theory [27]. A two-dimensional finite-volume method was used for the analysis. The grid size was 1 mm, and the time interval was 2 ps. The path distribution of photons that arrived at 2 ns is narrow and restricted to superficial media, whereas the photons detected at 20 ns are sensitive to deep layers. These results allow us to calculate weight functions for various diffuse optical tomography applications, which will be used in future studies.

2.10 Analysis of Spatially Resolved Measurement

To acquire quantitative measurements of the hemoglobin concentration in deep tissues by spatially resolved measurements, it is necessary to analyze the spatial intensity profile for a complex structure [28]. Figure 2.12 shows the increase in spatial slope because of increased absorption coefficient of muscle (μ_{am}) and increased fat layer thickness calculated in the Monte Carlo simulation. The model consisted of skin, fat, and muscle layers; the number of photons was 10^7. The spatial slope S was calculated by $\ln(I_{20}/I_{30})/(30–20)$, where I_{20} and I_{30} are the light intensities at 20 and 30 mm from the light source, respectively. It was found that fat thickness greatly affects determination of μ_{am}. For example, oxygenation measurements for a 3-mm fat layer decreased 30% if the $S - \mu_{am}$ curve of 9-mm fat thickness was used for quantification. The measurements were successfully corrected using the appropriate $S - \mu_{am}$ curve for fat thickness. The influence of millimeter inhomogeneity (e.g., layered structure) can be corrected using a combination of a diagnostic ultrasound

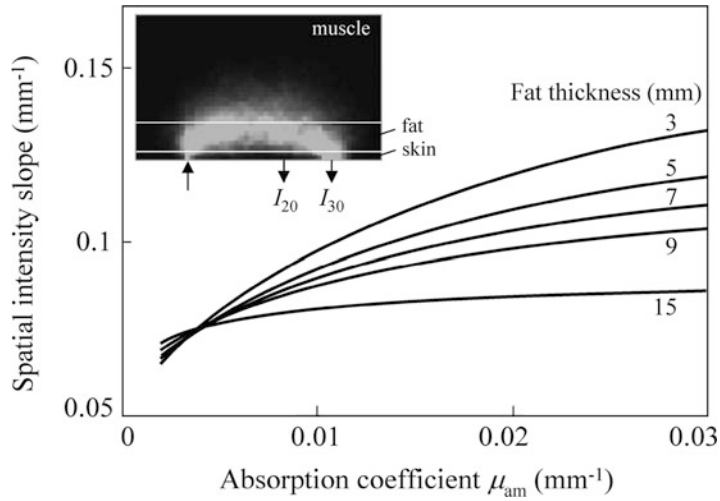

Fig. 2.12 Effect of fat thickness on the relationship between the slope of light intensity and the absorption coefficient of muscle

apparatus and NIRS instrument. Since the effects of micrometer inhomogeneity are reflected in the value of the scattering coefficient, estimation of the optical properties of each layer will be important for accurate oxygenation measurement.

Problem

2.1 A random number used on Monte Carlo simulation should be long period and of almost uniform distribution. How can this random number be generated?

Further Reading

Matsumoto M, Nishimura T (1998) Mersenne twister: a 623-dimensionally equidistributed uniform pseudorandom number generator. ACM Trans Model Comp Sim 8(1):3–30

Panneton F, L'Ecuyer P, Matsumoto M (2006) Improved long-period generators based on linear recurrences modulo 2. ACM Trans Math Softw 32:1–16

References

1. Chandraseklar S (1960) Radiative transfer. Dover, New York
2. Ishimaru A (1978) Diffusion of a pulse in densely distributed scatterers. J Opt Soc Am 68:1045–1050
3. Takatani S, Graham MD (1979) Theoretical analysis of diffuse reflectance from a two-layer tissue model. IEEE Trans Biomed Eng BME26:656–664
4. Patterson MS, Chance B, Wilson BC (1989) Time-resolved reflectance and transmittance for the noninvasive measurement of tissue optical properties. Appl Opt 28:2331–2336
5. Dayan I, Havlin S, Weiss GH (1992) Photon migration in a two-layer turbid media: a diffusion analysis. J Mod Opt 39:1567–1582
6. Farrell TJ, Patterson MS (1992) A diffusion theory model of spatially resolved, steady-state diffuse reflectance for the noninvasive determination of tissue optical properties in vivo. Med Phys 19:879–888
7. Haskell RC, Svaasand LO, Tsay TT, Feng TC, McAdams M, Tromberg BJ (1994) Boundary conditions for the diffusion equation in radiative transfer. J Opt Soc Am A 11:2727–2741

8. Kienle A, Patterson MS, Dögnitz N, Bays R, Wagnières G, van den Bergh H (1998) Noninvasive determination of the optical properties of two-layered turbid media. Appl Opt 37:779–791
9. Wilson BC, Adam G (1983) A Monte Carlo model for the absorption and flux distributions of light in tissue. Med Phys 10:824–830
10. van der Zee P, Delpy DT (1987) Simulation of the point spread function for light in tissue by a Monte Carlo method. Adv Exp Med Biol 215:179–191
11. Okada E, Firbank M, Delpy DT (1995) The effect of overlying tissue on the spatial sensitivity profile of near-infrared spectroscopy. Phys Med Biol 40:2093–2108
12. Wang L, Jacques S, Zheng L (1995) MCML—Monte Carlo modeling of light transport in multi-layered tissues. Comput Methods Programs Biomed 47(2):131–146
13. Yamamoto K, Niwayama M, Shiga T, Lin L, Kudo N, Takahashi M (1998) Accurate NIRS measurement of muscle oxygenation by correcting the influence of a subcutaneous fat layer. Proc SPIE 3194:166–173
14. Niwayama M, Lin L, Shao J, Kudo N, Yamamoto K (2000) Quantitative measurement of muscle hemoglobin oxygenation using near-infrared spectroscopy with correction for the influence of a subcutaneous fat layer. Rev Sci Instrum 71(12):4571–4575
15. Fang Q, Boas DA (2009) Monte Carlo simulation of photon migration in 3D turbid media accelerated by graphics processing units. Opt Express 17:20178–20190
16. Alerstam E, Svensson T, Andersson-Engels S (2008) Parallel computing with graphics processing units for high-speed Monte Carlo simulation of photon migration. J Biomed Opt 13:060504
17. Arridge SR, Schweiger M, Hiraoka M, Delpy DT (1993) A finite-element approach for modeling photon transport in tissue. Med Phys 20:299–309
18. Bonner R, Nossal R, Havlin S, Weiss H (1987) Model for photon migration in turbid biological media. J Opt Soc Am A 4:423–432
19. Nossal R, Kiefer J, Weiss GH, Bonner R, Taitelbaum H, Havlin S (1988) Photon migration in layered media. Appl Opt 27:3382–3391
20. Taitelbaum H, Havlin S, Weiss GH (1989) Approximate theory of photon migration in a two-layer medium. Appl Opt 28:2245–2249
21. Wan S, Anderson RR, Parrish JA (1981) Analytical modeling for the optical properties of skin with in vitro and in vivo applications. Photochem Photobiol 34:493–499
22. Beek JF, van Staveren HJ, Posthumus P, Sterenborg HJ, van Gemert MJ (1993) The influence of respiration on optical properties of piglet lung at 632.8 nm. In: Medical optical tomography. SPIE Optical Engineering Press, Bellingham, pp 193–210
23. Mitic G, Közer J, Otto J, Plies E, Sökner G, Zinth W (1994) Time-gated transillumination of biological tissues and tissuelike phantoms. Appl Opt 33:6699–6710
24. Zaccanti G, Taddeucci A, Barilli M, Bruscaglioni P, Martelli F (1995) Optical properties of biological tissues. Proc SPIE 2389:513–521
25. Wang ZY, Noyszewski EA, Leigh JS Jr (1990) In vivo MRS measurement of deoxymyoglobin in human forearms. Magn Reson Med 14:562–567
26. Harris RC, Hultman E, Kaijser L, Nordesjö LO (1975) The effect of circulatory occlusion on isometric exercise capacity and energy metabolism of the quadriceps muscle in man. Scand J Clin Lab Invest 35:87–95
27. Ueda Y, Ohta K, Yamashita Y, Tsuchiya Y (2003) Calculation of photon path distribution based on photon behavior analysis in a scattering medium. Opt Rev 10:444–446
28. Niwayama M, Sone S, Murata H, Yoshida H, Shinohara S (2007) Errors in muscle oxygenation measurement using spatially-resolved NIRS and its correction. J Jpn Coll Angiol 47:17–20

http://www.springer.com/978-1-4614-6251-4

Application of Near Infrared Spectroscopy in Biomedicine

Jue, Th.; Masuda, K. (Eds.)

2013, IX, 151 p., Hardcover
ISBN: 978-1-4614-6251-4